

RESEARCH ARTICLE | DECEMBER 13 2023

Numerical investigation of the tip-vortex-induced ventilation formation mechanism for a surface-piercing hydrofoil

Yuchang Zhi (支玉昌) ; Renfang Huang (黄仁芳)  ; Rundi Qiu (丘润荻); Yiwei Wang (王一伟) ; Qun Sun (孙群); Shuting Cai (蔡淑婷)



Physics of Fluids 35, 123328 (2023)

<https://doi.org/10.1063/5.0177292>



View
Online



Export
Citation

Articles You May Be Interested In

LES investigation into the cavity shedding dynamics and cavitation–vortex interaction around a surface-piercing hydrofoil

Physics of Fluids (December 2022)

Research on ventilation and supercavitation mechanism of high-speed surface-piercing hydrofoil

Physics of Fluids (February 2022)

Investigations into the ventilated cavities around a surface-piercing hydrofoil at high Froude numbers

Physics of Fluids (April 2022)



Physics of Fluids

Special Topics Open
for Submissions

[Learn More](#)

Numerical investigation of the tip-vortex-induced ventilation formation mechanism for a surface-piercing hydrofoil

Cite as: Phys. Fluids **35**, 123328 (2023); doi: 10.1063/5.0177292
Submitted: 20 September 2023 · Accepted: 21 November 2023 ·
Published Online: 13 December 2023






View Online



Export Citation



CrossMark

Yuchang Zhi (支玉昌),¹  Renfang Huang (黄仁芳),^{2,a)}  Rundi Qiu (丘润荻),^{2,3} Yiwei Wang (王一伟),^{2,3,4} 
Qun Sun (孙群),¹ and Shuting Cai (蔡淑婷)^{2,4}

AFFILIATIONS

¹School of Mechanical and Automotive Engineering, Liaocheng University, Liaocheng 252000, China

²Key Laboratory for Mechanics in Fluid Solid Coupling Systems, Institute of Mechanics, Chinese Academy of Sciences, Beijing 100190, China

³School of Future Technology, University of Chinese Academy of Sciences, Beijing 100049, China

⁴School of Engineering Science, University of Chinese Academy of Sciences, Beijing 100049, China

^{a)} Author to whom correspondence should be addressed: hrenfang@imech.ac.cn

ABSTRACT

Recent experiments have demonstrated that tip vortices can trigger the ventilation formation around a surface-piercing hydrofoil. However, the influence of this ventilation on transient flow structures and vortex evolution remains unresolved. This paper numerically investigates the tip-vortex-induced ventilation formation for a surface-piercing hydrofoil at a stalled yaw angle. The predicted unsteady ventilated cavities with tip vortices and pressure-side spray are in reasonable agreement with experimental observations. The ventilation formation process can be divided into three stages: base ventilation, tip-vortex ventilation, and suction-side ventilation. It is indicated that ventilation has a greater impact on the lift coefficient than the drag coefficient. The lift coefficient increases during the base ventilation and tip-vortex ventilation stages due to the expansion of the low-pressure stalled flow, but decreases in the suction-side ventilation stage because of the gradual replacement of this low-pressure region by an aerated cavity. Tip-leakage and tip-separation vortices initially exist independently at the hydrofoil tip, then expand and merge through air ventilation, ultimately forming a strongly stable tip vortex. Furthermore, ventilation promotes vortex generation, with the major contributors being the vortex stretching and baroclinic torque terms.

Published under an exclusive license by AIP Publishing. <https://doi.org/10.1063/5.0177292>

I. INTRODUCTION

High-speed unmanned ships have emerged as a vital element in future ocean systems, offering the potential for lower costs, mitigated risks, and enhanced flexibility and efficiency across a range of tasks and applications.^{1–3} This includes a novel category of vessels known as hydrofoil ships, which utilize hydrofoils as integral lift components that allow the hull to be elevated above the water surface.⁴ Consequently, the overall resistance encountered by hydrofoil ships is significantly reduced, enabling them to achieve high speeds while sailing across the surface of the water.^{5–7}

As the hydrofoil operates in two different fluids, namely, air and water, a downward pressure difference occurs at the air–water interface. This pressure difference causes air to flow toward the low-pressure water area, forming an aerated cavity on the suction side (SS) of the hydrofoil. This phenomenon is called ventilation, and the

resulting air cavity is referred to as a ventilated cavity. Ventilation profoundly affects the hydrofoil's hydrodynamic performance due to the replacement of water with air on the suction surface.⁸ Further advances in hydrofoil technology will undoubtedly depend on controlling the formation of ventilation. Consequently, studying the mechanism of ventilation formation will help us better understand its effects and how to utilize ventilation to improve the hydrodynamic performance of hydrofoils.

Since 1950, numerous experimental studies have investigated the ventilation formation mechanisms, leading to a comprehensive understanding of the various hydrofoil ventilation modes. In 1959, Breslin and Skalak⁹ performed experiments using a surface-piercing hydrofoil. They observed that air enters the tip vortex from the hydrofoil's trailing edge (TE) and ventilates the hydrofoil's leading edge (LE) through the tip vortex, which is called “tip-vortex-induced ventilation.”^{9,10}

Using particle image velocimetry, Pogozelski *et al.*¹¹ observed that when waves near the hydrofoil interfere with the free surface, vortex structures are generated that destroy the free surface sealing, causing air entrainment at the hydrofoil's suction surface. This ventilation mode is called "stall-induced ventilation." Rothblum¹² found that, under a high Froude number and an appropriate angle of attack, the Taylor instability of the free surface also causes air to occupy the hydrofoil's SS. This ventilation mode is referred to as "tail ventilation." The hydrofoil's suction surface experiences vaporous cavitation due to low pressure at high Froude numbers.^{13–15} Due to the extremely low pressure inside the cavity, even a minor disturbance can rapidly introduce air into the vaporous cavity, leading to ventilation formation. This ventilation mode is known as "cavitation-induced ventilation." Recently, a series of ventilation experiments have been conducted by Harwood *et al.* at low and medium Froude numbers.^{16–18} They have extensively explored various ventilation modes and fully described the characteristics of the flow regime during the ventilation process. Through their experiments, they have provided extensive insight into the ventilation formation mechanisms¹⁷ and have identified stable regions in the parameter space for fully wetted (FW) flow, fully ventilated (FV) flow, and partially ventilated (PV) flow. Subsequently, they conducted experiments to investigate the hydroelastic response of a hydrofoil in wetted, ventilating, and cavitating flows.^{19,20} Huang *et al.* carried out numerous experiments in a constrained-launching water tank and have extended their insight to the transition mechanisms of flow regimes at high Froude numbers.^{10,21} They found that only the FW and FV states exist at high speeds. On this basis, Wang *et al.* studied the ventilation mechanism induced by cavitation together with a water surface depression and proposed a criterion for this type of ventilation formation.²² The tip-vortex cavitation, along with the torque and noise, were experimentally analyzed for a pitching hydrofoil under static and dynamic angles of attack (AoAs).²³ Another study generated periodic bubbling cavitation from a Harvey-type crevice in a Venturi experimental section and showed that the cavitation frequency strongly depends on the non-condensable gas content, indicating that this cavitation phenomenon is driven by gas diffusion.²⁴

Numerical research has also been used to obtain details about the ventilating flow of a surface-piercing hydrofoil.²¹ With advances in high-performance computing, many scholars^{25–27} have employed CFD to simulate the ventilation phenomena of hydrodynamic devices, yielding promising and satisfactory results. Charlou *et al.* studied the ventilation inception and stability under bistable conditions through the Reynolds-averaged Navier–Stokes method with a Cartesian grid.²⁸ The simulated results were found to be in good agreement with experimental data, demonstrating that the transient mechanism is the reason for ventilation inception. This underscores the importance of studying transient mechanisms in the process of unsteady ventilation. Matveev *et al.*²⁹ used the STAR-CCM+ software to perform numerical simulations on hydrofoils with varying yaw angles as a means of studying ventilation phenomena. The calculated results exhibited satisfactory agreement with experiments. Their study revealed that using the $k-\epsilon$ turbulence model together with grid refinement near the hydrofoil LE and the free surface can effectively simulate the unsteady cavitating flow during the ventilation process. Various simulation schemes (e.g., turbulence intensity, time step, interface capture scheme) have been used to simulate surface-piercing hydrofoils.^{10,30–32} The results indicate that adopting a reasonable time step and grid refinement are helpful in

predicting the ventilation flow characteristics. Zhi *et al.* investigated the ventilation elimination when a plate hydrofoil pierces the water surface under deceleration, demonstrating that the stability of a ventilated cavity is strongly dependent on the reentrant jet.^{10,32} Zhi *et al.* studied the cavitation shedding dynamics of a surface-piercing hydrofoil using large-eddy simulations (LES), with an emphasis on the cavitation–vortex interaction.³³ Wang *et al.* simulated the flow structures around a semi-ogive hydrofoil at various angles of attack and analyzed the interaction between natural supercavitation and ventilation, finding that the lift coefficient is reduced by half when supercavitation transitions into a fully ventilated flow.³⁴ Li *et al.* proposed a high-fidelity LES framework that accurately captures the turbulent ventilated flow around a surface-piercing hydrofoil.³⁵ To capture the shock waves induced by bubble collapse and rebound, Nguyen *et al.* developed a high-resolution Riemann solver that considers both compressibility and mass transfer during phase-change transitions.³⁶ Zhang *et al.* analytically studied the free oscillation of a single bubble in a narrow gap in comparison with that in an infinite liquid, demonstrating that the former is significantly influenced by the bubble radius.³⁷

Based on the above literature review, numerous scholars have conducted studies on the gas–water two-phase flow around a surface-piercing hydrofoil through experiments and calculations, including the transition mechanisms of flow patterns, hydroelastic responses, and vaporous cavitation effects on ventilation.³³ Although tip-vortex-induced ventilated cavities can be experimentally observed, it is difficult to obtain quantitative information on the aerated flow field using existing measurement techniques. Additionally, there are a few reports on the tip-vortex-induced ventilation dynamics and their formation mechanism, and the correlation between ventilation and the associated flow structures is still unclear. Therefore, the present paper numerically investigates the ventilation formation mechanism induced by tip vortices. The transient evolution of gas ventilation and its associated hydrodynamic fluctuations are analyzed in depth. A particular emphasis is directed toward understanding the correlation and influence of ventilation on the flow structures and vortex evolution.

II. SIMULATION APPROACH

A. Governing equations

The homogenous equilibrium flow assumption is employed herein for solving the two-phase flow with the following governing equations:³⁸

$$\frac{\partial \rho_m}{\partial t} + \frac{\partial (\rho_m u_i)}{\partial x_i} = 0, \tag{1}$$

$$\begin{aligned} & \frac{\partial (\rho_m u_i)}{\partial t} + \frac{\partial (\rho_m u_i u_j)}{\partial x_j} \\ & = - \frac{\partial p}{\partial x_i} + \frac{\partial}{\partial x_j} \left((\mu_m + \mu_t) \left(\frac{\partial u_i}{\partial x_j} + \frac{\partial u_j}{\partial x_i} - \frac{2}{3} \frac{\partial u_k}{\partial x_k} \delta_{ij} \right) \right), \end{aligned} \tag{2}$$

where u_i is the velocity component in the i -direction, p is the mixture pressure, μ_t is the turbulent viscosity, ρ_m is the mixture density, and μ_m is the laminar viscosity.³⁹ The mixture properties are calculated by volume-weighted averaging of each phase according to

$$\rho_m = \alpha_a \rho_a + (1 - \alpha_a) \rho_l, \tag{3}$$

$$\mu_m = \alpha_a \mu_a + (1 - \alpha_a) \mu_l, \tag{4}$$

where α is the volume fraction, and the subscripts l and a represent liquid water and air, respectively.⁴⁰

The realizable k - ε turbulence model is adopted to ensure the closure of the μ_t expression for turbulent flows.⁴¹ μ_t is calculated by $\mu_t = \rho_m C_\mu f_\mu k T$, where C_μ is a model coefficient ($C_\mu = 0.09$), f_μ is a damping function, and T is the turbulent timescale. This is the large-eddy timescale (T_e) given by⁴²

$$T = T_e = \frac{k}{\varepsilon}. \quad (5)$$

The transport equations for the turbulent kinetic energy k and the turbulent dissipation rate ε are

$$\frac{\partial}{\partial t}(\rho_m k) + \nabla \cdot (\rho_m k \bar{\mathbf{u}}) = \nabla \cdot \left[\left(\mu_m + \frac{\mu_t}{\sigma_k} \right) \nabla k \right] + P_k - \rho_m (\varepsilon - \varepsilon_0), \quad (6)$$

$$\begin{aligned} \frac{\partial}{\partial t}(\rho_m \varepsilon) + \nabla \cdot (\rho_m \varepsilon \bar{\mathbf{u}}) = \nabla \cdot \left[\left(\mu_m + \frac{\mu_t}{\sigma_\varepsilon} \right) \nabla \varepsilon \right] \\ + \frac{1}{T_e} C_{e1} P_\varepsilon - C_{e2} f_2 \rho_m \left(\frac{\varepsilon}{T_e} - \frac{\varepsilon_0}{T_0} \right), \end{aligned} \quad (7)$$

where $\bar{\mathbf{u}}$ is the mean velocity, σ_k , σ_ε , C_{e1} , and C_{e2} are model coefficients,⁴² $f_2 = \frac{k}{k + \sqrt{\nu \varepsilon}}$ is a damping function, and ε_0 represents the ambient turbulence value to offset turbulence attenuation.^{43,44} Furthermore, to add an ambient source term, the specific timescale T_0 is defined in Eq. (8),⁴⁵ where $C_t = 1$ is a model coefficient and ν is the kinematic viscosity.

$$T_0 = \max \left(\frac{k_0}{\varepsilon_0}, C_t \sqrt{\frac{\nu}{\varepsilon_0}} \right). \quad (8)$$

In Eqs. (6) and (7), P_k and P_ε are production terms given by

$$P_k = f_c G_k + G_b - \gamma_M, \quad (9)$$

$$P_\varepsilon = C_{e3} G_b, \quad (10)$$

where G_k and G_b are production terms that consider turbulence and buoyancy, respectively, and γ_M is the compressibility modification.⁴² C_{e3} is a model coefficient, and f_c is the curvature correction factor.

As regards the wall function, on the cell closest to the profile, a two-layer model approach is applied. This imposes a first thin laminar layer near the wall and a second logarithmic layer over the first and assumes that the centroid of the first cell near the wall lies within the logarithmic region of the boundary layer.

B. Wave damping

Wave damping is applied at the outlet and lateral planes in numerical simulations³³ to avoid wave reflection. Specifically, the following resistance term is introduced to the vertical velocity component (w -velocity):⁴⁶

$$S_z^d = \rho_m (m_1 + m_2 |w|) \frac{e^\kappa - 1}{e^\kappa + 1} w, \quad (11)$$

$$\kappa = \left(\frac{x - x_{sd}}{x_{ed} - x_{sd}} \right)^{n_d}. \quad (12)$$

In this context, x_{sd} and x_{ed} represent the starting and end points for wave damping, respectively, and m_1 , m_2 , and n_d are model parameters that can be found in Ref. 46.

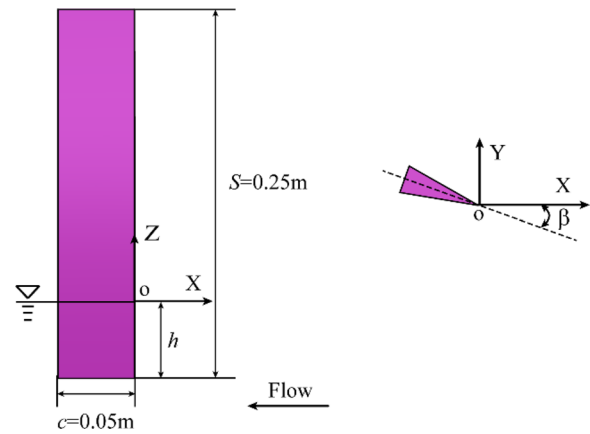


FIG. 1. Hydrofoil geometry.

C. Hydrofoil geometry

A plate hydrofoil (Fig. 1) is selected, as used in a great many experiments with a constrained launch experimental system.²¹ The hydrofoil has an isosceles triangular cross section along the spanwise direction with a vertex angle of 20° ,³³ so the foil trailing edge is blunt. This study focuses on the ventilation formation caused by the tip vortex. The geometrical parameters and operation conditions (Table I) are consistent with the experimental conditions, that is, the yaw angle is $\beta = 20^\circ$, the immersed aspect ratio is $AR_h = 1.5$, and the hydrofoil speed gradually increases in the range of 0.8–2.7 m/s relative to the incoming flow, corresponding to depth Froude numbers of $Fr_h = 0.93$ –3.15. Velocity variations are considered in the present simulations. Minor changes in velocity are often neglected and treated as part of a uniform motion in high-speed surface-piercing conditions.

D. Computational domain, boundary conditions and numerical setup

To mirror the experimental setup, Fig. 2 depicts the computational domain, which ranges from $[10c, -20c]$ in the X-direction, from $[-5c, 5c]$ in the Y-direction, and from $[5c, -10c]$ in the Z-direction. A time-varying velocity profile is set at the inlet boundary, which matches the magnitude of the velocity experienced by the hydrofoil in the experiment. For the pressure outlet boundary, a hydrostatic pressure distribution is applied, corresponding to a flat volume-of-fluid wave.³³ The pressure is set to $P_{atm} = 101325$ Pa at the free surface. The other surfaces are set as no-slip wall boundaries, implying that the flow

TABLE I. Geometrical parameters and operation conditions.

Chord length	c	0.05 m
Span	S	0.25 m
Tip immersion	h	0.075 m
Yaw angle	β	20°
Immersed aspect ratio	$AR_h = \frac{h}{c}$	1.5
Velocity	u_∞	0.8–2.7 m/s
Depth Froude number	$Fr_h = \frac{u_\infty}{\sqrt{gh}}$	0.93–3.15

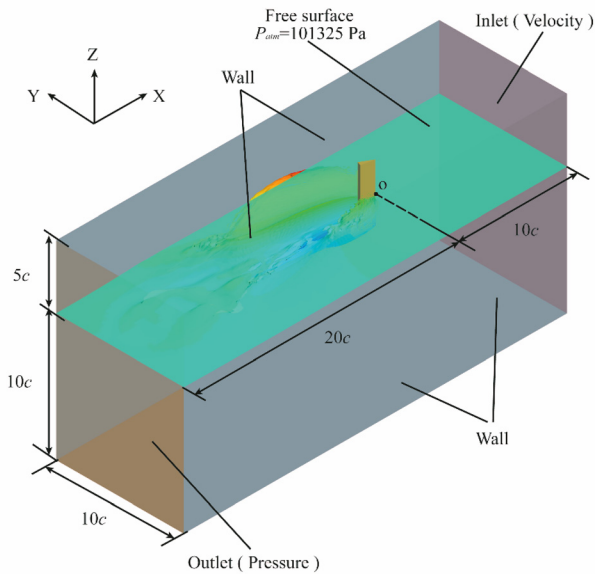


FIG. 2. Computational domain.

velocity is zero at these surfaces, following the solid boundary conditions. By implementing these boundary conditions, we effectively replicate the experimental setup with the aim of accurately simulating the transient ventilation phenomenon.

For the volume-of-fluid solution, we employ the high-resolution interface capturing scheme.³³ The time step is set to $\Delta t = 0.0001$ s. This numerical method has been used in many similar studies and has been proven to accurately reproduce the cavity evolution with free surface deformation.

E. Mesh generation

The mesh quality and resolution are crucial in accurately predicting the behaviors of ventilated cavities. To achieve a more precise representation of the ventilation flow field, we utilize a high-quality Cartesian grid together with the control volume method to effectively

capture the flow dynamics around the hydrofoil. The meshing process is illustrated in Fig. 3.

Initially, a surface remesher is applied on the hydrofoil suction surface and pressure surface, generating a high-quality surface mesh with good surface triangulation.³³ Subsequently, a prism layer mesh and trimmed mesh are generated based on the surface mesh. The mesh around the foil wall has 32 layers and a growth rate of 1.2, with a total thickness of 0.0015 m, as shown in Fig. 3(c). To satisfy algorithmic requirements,^{26,28,29} y^+ is less than 30.

The refined grid around the hydrofoil enables a more accurate simulation of the flow regime within the aerated cavity and the free surface. Using this mesh setup enhances the reliability and accuracy of our simulation results, allowing for a comprehensive understanding of the complex flow dynamics that occur during ventilation formation.

F. Numerical verification

Three meshes are used to investigate the grid independence. In the following, the subscripts 1, 2, and 3 correspond to coarse, medium, and fine meshes, respectively. The lift coefficient (C_L) and drag coefficient (C_D) are calculated at a specified condition ($Fr_h = 3.15$, $AR_h = 1.5$, $\beta = 20^\circ$). These coefficients are defined as

$$C_L = \frac{L}{0.5\rho_m u_\infty^2 hc}, \quad C_D = \frac{D}{0.5\rho_m u_\infty^2 hc}. \quad (13)$$

To assess the mesh independence, the grid convergence index (GCI) method⁴⁷⁻⁴⁹ is employed. The GCI for the fine mesh can be defined as

$$GCI_{32} = \frac{F_s |\epsilon_{32}|}{\tau^\chi - 1}, \quad (14)$$

where F_s is the safety factor ($F_s = 1.25$), ϵ_{32} is the relative error ($\epsilon_{32} = \zeta_3 - \zeta_2$, where ζ represents C_L or C_D), τ is the mesh refinement ratio ($\tau = N_3/N_2 = 2$, where N is the grid number), and χ indicates the convergence order, obtained as

$$\chi = \ln\left(\frac{\zeta_3 - \zeta_2}{\zeta_2 - \zeta_1}\right) / \ln(\tau). \quad (15)$$

The GCI values for C_L and C_D are presented in Table II. For C_L , the GCI between the medium and coarse meshes is $GCI_{21} = 0.83\%$,

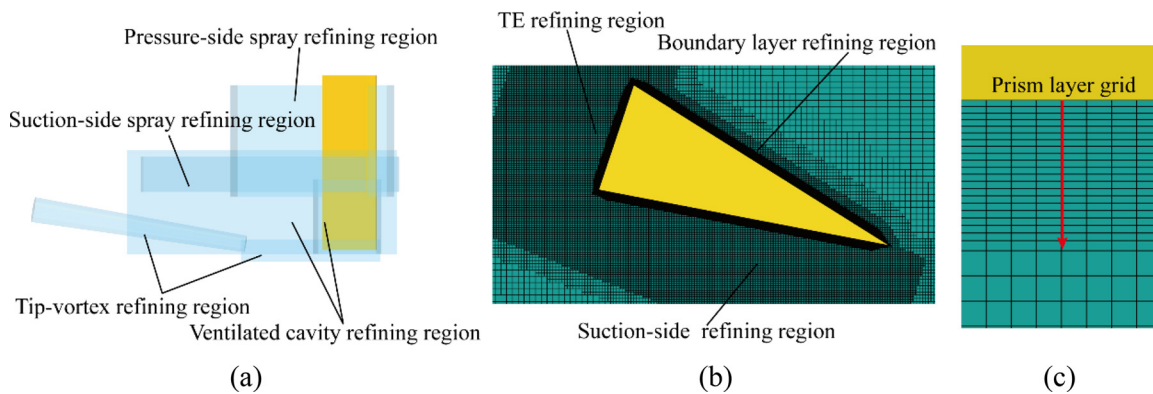


FIG. 3. Meshing details: (a) refined region, (b) refined region around the foil, and (c) prism layer grid.

TABLE II. Mesh convergence study.

	Grid nodes ($\times 10^6$)	C_L	GCI- C_L	C_D	GCI- C_D
Mesh 1	9.20	0.064 073	...	0.043 704	...
Mesh 2	18.40	0.063 764	GCI ₂₁ = 0.83%	0.043 992	GCI ₂₁ = 1.00%
Mesh 3	36.80	0.064 298	GCI ₃₂ = 1.44%	0.044 517	GCI ₃₂ = 1.81%

while that between the fine and medium meshes is $GCI_{32} = 1.44\%$. For C_D , the GCI between the medium and coarse meshes is $GCI_{21} = 1.00\%$ and that between the fine and medium meshes is $GCI_{32} = 1.81\%$. This indicates that the results using the various grid resolutions are very similar for both C_L and C_D . With the value of $\chi \approx 0.789$ herein, we have that $GCI_{32} \approx \tau^2 \cdot GCI_{21}$, which demonstrates that the solutions using these three grid resolutions are within the scope of asymptotic convergence.³³ Using the Richardson extrapolation method, it can be inferred that when GCI is less than 5%, the simulated results obtained from mesh 3 are grid-independent. Therefore, subsequent simulations are performed using the grid generated by mesh 3. This approach ensures that the numerical results are reliable and not significantly influenced by the grid resolution.

III. RESULTS AND DISCUSSION

A. Flow characteristics during the formation of tip-vortex-induced ventilation

Figure 4 illustrates the ventilated cavities at various instants, as observed in the experiments and computed by the numerical scheme. The numerical results visualize the air–water interface using an isosurface with a water fraction threshold of 0.5. These calculated results are in reasonable agreement with the experimental observations.

The numerical simulations capture the ventilated cavity on the SS together with the pressure-side (PS) spray at various stages in the ventilation process. Particularly noteworthy is the prominent presence of a tip vortex that actively absorbs air from the base cavity aft of the hydrofoil's TE.

Four different flow regimes have been identified throughout the ventilation formation process: base ventilated (BV) flow, tip-vortex ventilated (TVV) flow, suction-side ventilated (SSV) flow, and fully ventilated (FV) flow. The multiphase flow characteristics at these different stages are described as follows:

Base ventilated (BV) flow: An aerated cavity forms in the separated flow behind the hydrofoil's TE, primarily confined to the aft section of the blunt TE. The pressure is higher on the PS than on the SS, causing the free surface to deform into small water spray sheets [Figs. 4(a)–4(c)].

Tip-vortex ventilated (TVV) flow: The hydrofoil's TE is entirely enclosed within the BV cavity. The vortex at the hydrofoil tip continuously entrains air due to its low pressure, promoting the accumulation of gas at the hydrofoil tip and forming an aerated tip vortex, as shown in Figs. 4(d) and 4(e).

Suction-side ventilated (SSV) flow: Due to the presence of sufficiently stable aerated tip vortices, air can be continuously supplied from the wake. Therefore, the cavity rapidly expands toward the free surface and the hydrofoil TE, exhibiting an upward-sloping trajectory, as depicted in Figs. 4(f)–4(h).

Fully ventilated (FV) flow: The hydrofoil's submerged portion is entirely enclosed within the ventilated cavity. Large water spray sheets form on both sides and there is a strong tip vortex. The FV flow remains stable, as shown in Fig. 4(i).

Based on the findings from experiments and numerical simulations, the three stages in the ventilation formation process are illustrated in Fig. 5.

First stage: Base ventilation formation, shown in Fig. 5(a). At the hydrofoil's TE, air ventilation is initiated as the hydrofoil accelerates, leading to the formation of an aerated cavity behind the hydrofoil. As the speed of the hydrofoil increases, air begins to penetrate downward along the hydrofoil's blunt TE.

Second stage: Tip-vortex ventilation formation, shown in Fig. 5(b). As the hydrofoil speed continues to increase, air enters the tip vortex, forming an aerated vortex core. The air continues to flow upstream along the tip, and finally arrives at the hydrofoil's LE.

Third stage: Suction-side ventilation formation, shown in Fig. 5(c). Once the aerated cavity reaches the LE, it quickly expands upward along the hydrofoil's suction surface, forming FV flow. The ventilation process suffers a rapid transition from partially ventilated state to a fully ventilated state.

These three stages describe the process of ventilation formation during the acceleration of the hydrofoil, starting from base ventilation and moving through tip-vortex ventilation and suction-side ventilation, before culminating in a fully ventilated flow, which completely envelops the hydrofoil.

The shape of the pressure-side spray given by the experimental measurements and calculations at different instants is compared in Fig. 6, as extracted from the digital images using an in-house MATLAB code. First, from the grayscale digital image, the shape of the PS spray is determined using an edge detection method in MATLAB. Second, calibration is performed using a rectangular template pasted on the surface-piercing hydrofoil. Thus, the pixel coordinate values of the spray shape can be converted to actual coordinate values. The ordinate represents the dimensionless height of the PS spray, and the abscissa represents the dimensionless distance from the hydrofoil. By analyzing the shape evolution of the PS spray at different instants, the following conclusions can be drawn.

The free surface near the hydrofoil's PS rises on account of the high stagnation pressure at the hydrofoil's LE and the large pressure gradient on the pressure surface, thereby forming a PS spray. The PS spray behind the hydrofoil's TE initially rises, forming a wave crest, then descends while interacting with the free surface in the far field. As the hydrofoil speed increases, the crest position of the PS spray gradually moves backward, the crest height increases, and the transverse length of the PS spray increases. This is because higher hydrofoil speeds lead to greater hydrofoil momentum acting on the free surface.

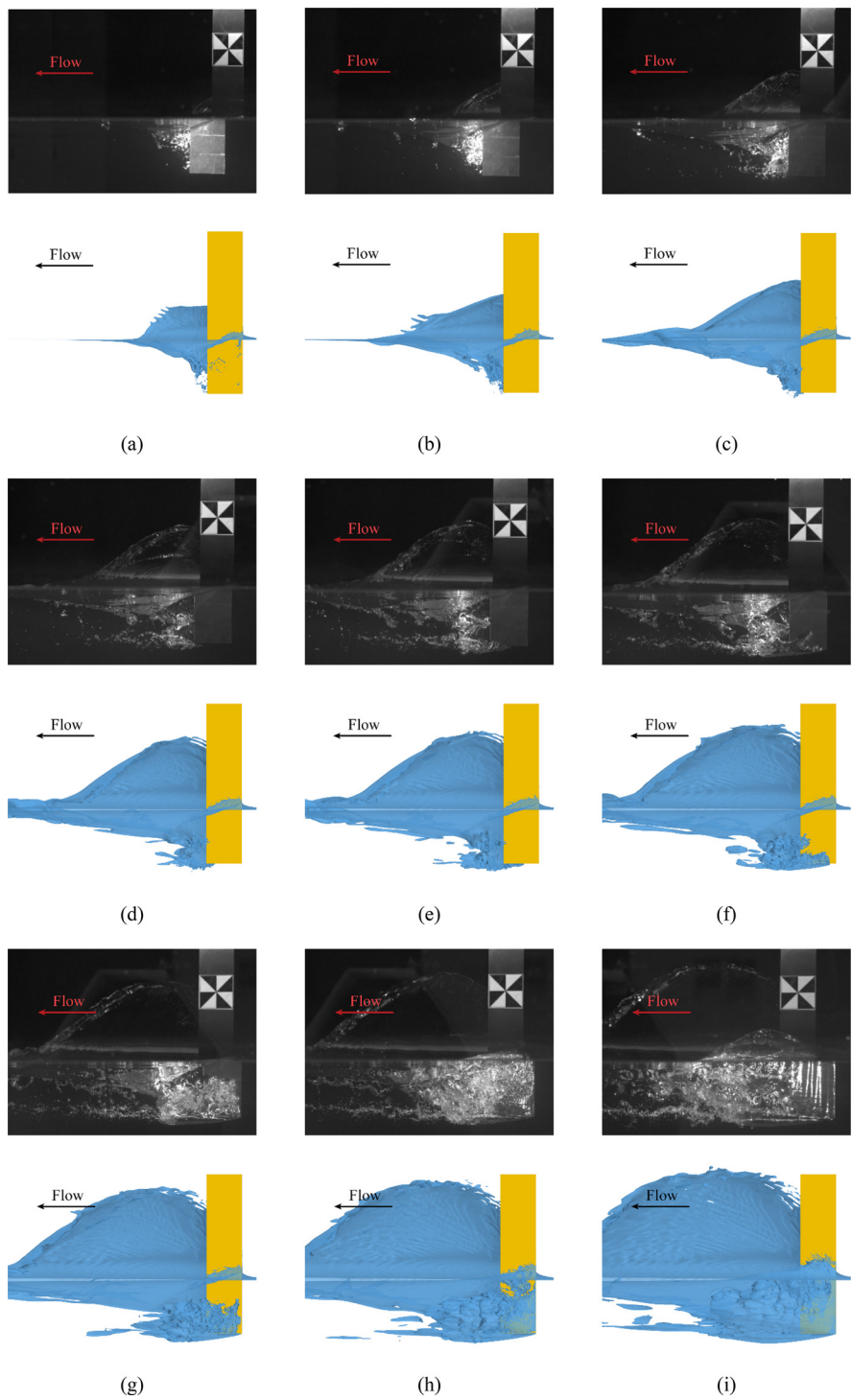


FIG. 4. Evolution of ventilated cavity shape (upper: experiment, lower: CFD): (a) t_0 , (b) $t_1 = t_0 + 0.05$ s, (c) $t_2 = t_0 + 0.1$ s, (d) $t_3 = t_0 + 0.15$ s, (e) $t_4 = t_0 + 0.175$ s, (f) $t_5 = t_0 + 0.2$ s, (g) $t_6 = t_0 + 0.225$ s, (h) $t_7 = t_0 + 0.25$ s, and (i) $t_8 = t_0 + 0.3$ s.

The PS spray shape obtained from the calculations is in good agreement with the measured data. However, at higher hydrofoil speeds, the calculated PS spray shape exhibits larger errors. In the calculations, we consider the effect of gravity. The quality of the mesh is

critical to accurately capture the free surface. The mesh should have sufficient resolution near the fluid surface to effectively capture the shape and motion of the free surface. This article focuses on the tip-vortex-induced ventilation of the hydrofoil's underwater portion, so

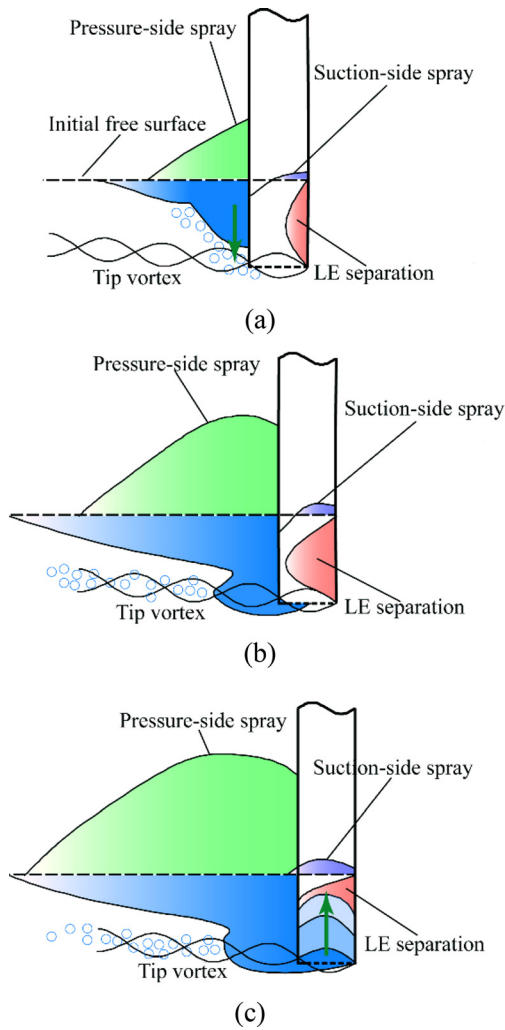


FIG. 5. Three stages of the tip-vortex-induced ventilation formation: (a) base ventilation, (b) tip-vortex ventilation, and (c) suction-side ventilation.

the far-field grid is coarser than that around the hydrofoil. In regions where the mesh resolution is large, therefore, the gas-liquid interface position and shape will have large errors. These discrepancies can be attributed to insufficient mesh resolution in this portion of the PS spray. Increasing the mesh resolution above the free surface and behind the hydrofoil would undoubtedly lead to more accurate PS spray shapes but would also significantly increase the computational cost. Consequently, the current mesh is chosen based on computing requirements, striking a balance between the calculation accuracy and efficiency.

B. Hydrodynamic load coefficients

Throughout the ventilation formation process, the hydrofoil undergoes acceleration, as illustrated in Fig. 7. The speed input of the hydrofoil for the numerical calculations is extracted from the experimental data. Figure 8 illustrates the variations in C_L and C_D during the

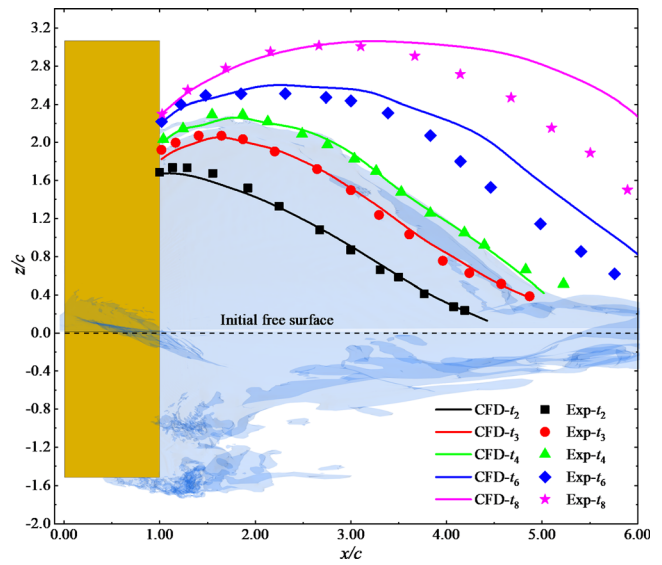


FIG. 6. Comparison of pressure-side spray shape between experiment (Exp) and simulation (CFD).

acceleration process. Regions I, II, III, and IV correspond to the four flow patterns described in Sec. III A, i.e., BV flow [Figs. 4(a)–4(c)], TVV flow [Figs. 4(d) and 4(e)], SSV flow [Figs. 4(f)–4(h)], and FV flow [Fig. 4(i)], respectively.

C_L and C_D increase as the hydrofoil speed rises in the BV and TVV regimes. In these regimes, the ventilated cavity is limited to the area near the hydrofoil TE and tip. The cavity slightly affects the pressure distribution at the hydrofoil’s surface, so the ventilated cavity does not obviously affect the hydrodynamic loads. In contrast, as the hydrofoil speed increases, the separation region on the hydrofoil’s SS expands, resulting in a faster increase in C_L . On the contrary, the drag coefficient increases more slowly.

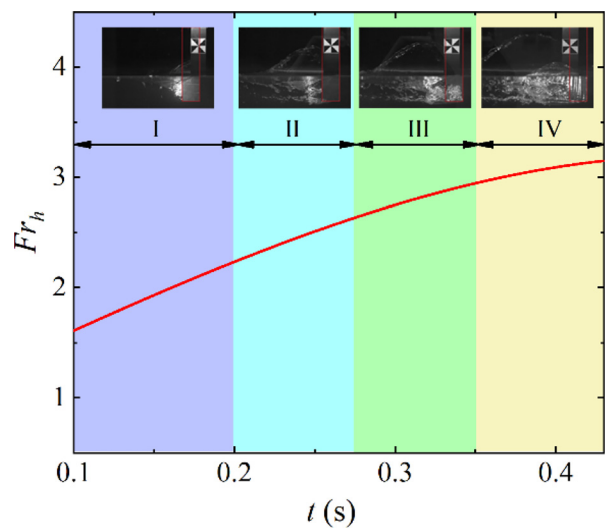


FIG. 7. Time history of the hydrofoil speed.

21 October 2024 06:19:15

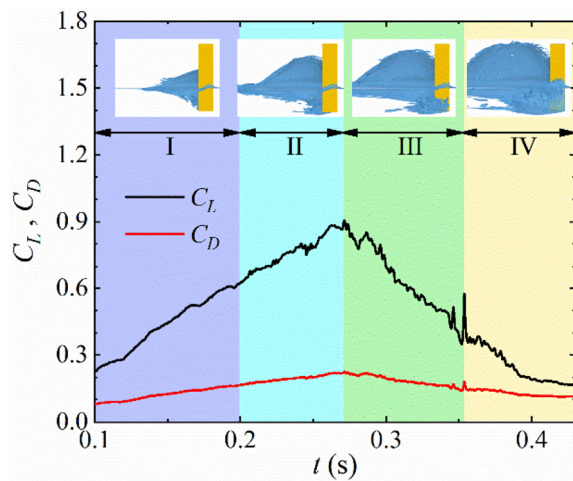


FIG. 8. Time history of the hydrofoil lift coefficient (C_L) and drag coefficient (C_D).

When the ventilation flow regime transitions from TVV to SSV, C_L and C_D decrease as the hydrofoil speed rises. In the SSV flow regime, a portion of the hydrofoil's SS is covered by the aerated cavity. As the ventilated cavity is open to the surrounding environment, the hydrofoil portion covered by the ventilated cavity is under atmospheric pressure, causing a reduction in the pressure difference on both sides of the hydrofoil together with a reduction in the lift coefficient.

In the FV regime, C_L first decreases and then remains unchanged with increasing hydrofoil speed. The reason for the decrease can be partially attributed to the long cavity of each section along the span. The longer cavity contributes to a more significant interaction between the aerated cavity and the surrounding flow, causing a reduction in the lift coefficient as the hydrofoil speed increases. Finally, the lift coefficient remains unchanged when the cavity length stabilizes in the FV flow.

C. Correlation between ventilation and flow structures

Figure 9 illustrates the pressure distribution near the hydrofoil at various instants using the resampled volume rendering technique. This technique utilizes voxels, which are three-dimensional pixels representing the volume. Throughout the ventilation formation process, three distinct low-pressure regions can be observed around the hydrofoil: the TE low-pressure region (LPR), the tip LPR, and the LE LPR. The pressure distribution around the hydrofoil is analyzed as follows.

In Fig. 9(a), a typical TE LPR is observed aft of the hydrofoil. As the air enters and forms a basic cavity at the hydrofoil tail [see Figs. 4(a)–4(c)], the TE LPR decreases in size [Figs. 9(a) and 9(b)], and then disappears [Figs. 9(c)–9(i)]. This is because air ventilation significantly increases the pressure at the TE, leading to a transition from low pressure to standard atmospheric pressure.

There is an area of low pressure in the tip vortex [Figs. 9(a)–9(e)]. This creates a natural pressure difference relative to atmospheric pressure, which promotes the continuous transport of atmospheric gas from the base cavity to the hydrofoil tip [Figs. 9(c)–9(e)], accompanied by the gradual disappearance of the tip LPR. This corresponds to tip-vortex ventilation formation in Fig. 5(b).

Figure 9(a) shows that the LE LPR exhibits a parabolic shape. The reduction in the LPR length toward the hydrofoil tip is attributed to an augmentation in static pressure.⁵⁰ The reduction in length toward the free surface is caused by the free surface effect, which diminishes the effective yaw angle.³¹ In addition, the yaw angle $\beta = 20^\circ$, exceeding the stall angle, so the flow separation corresponds to the LPR on the hydrofoil's SS. The LE LPR expands toward the hydrofoil TE with increasing speed, enlarging the separation region and providing a favorable pressure gradient for ventilation. During the SSV stage [Figs. 9(f)–9(h)], the hydrofoil's SS is occupied by the aerated cavity and reaches standard atmospheric pressure due to air ventilation, eventually subjecting the entire suction surface to standard atmospheric pressure [Fig. 9(i)].

The air-ventilated path is connected to the LPRs. At the interface with the free surface, the air maintains atmospheric pressure, while the underwater region experiences significantly lower pressure. This pressure difference pushes air to enter the LPRs in the water. Hydrofoil base ventilation can also occur at lower hydrofoil speeds, and the depth of cavity ventilation generally relates to the geometric shape and Froude number.

The low pressure generated by flow separation can affect ventilation.¹⁵ The TE LPR is generated by flow separation at the hydrofoil TE, and the LE LPR is formed by flow separation at the hydrofoil LE (Fig. 10). The tip LPR is attributed to the presence of the tip vortex, which arises from the pressure difference between the hydrofoil's PS and SS (Fig. 11).⁵¹

The TE flow separation, tip cross-flow, and LE flow separation are further analyzed by examining the detailed flow fields around the hydrofoil. This analysis involves extracting cross-sectional views at various positions near the hydrofoil, as depicted in Fig. 12. By examining these cross-sectional views, a more comprehensive understanding of the factors contributing to flow separation can be obtained.

Figures 13 and 14 show the streamline, velocity, and pressure distributions of the cross-sectional positions ($z = 1/3h$ and $z = 4/5h$) at time t_0 . Analysis of these distributions reveals several key observations.

A local high-pressure region appears at the hydrofoil PS; in contrast, there is an LPR at the hydrofoil's SS. Near both the hydrofoil LE and TE, there are regions of low velocity and low pressure. The streamline distribution in these regions shows complex flow patterns, including backflow and vortices (Fig. 14). These phenomena are the result of water decelerating in the boundary layer under the integrated effects of a pressure difference and viscosity. This causes the mainstream flow to deviate from the hydrofoil boundary layer, forming low-velocity and low-pressure separation regions at the hydrofoil LE and TE. Comparing the velocity distributions at the $z = 1/3h$ and $z = 4/5h$ cross sections (Fig. 14), as the depth increases, the size of the separation region at the hydrofoil LE decreases. This reduction is caused by the enhancement in local pressure, which is in turn caused by the increase in hydrostatic pressure as the depth increases (Fig. 13).

Flow separation is significantly influenced by the geometry and Froude number of the hydrofoil. In our experiments and calculations involving a flat hydrofoil, the presence of a blunt TE makes it more susceptible to flow separation at that specific location. Additionally, as the yaw angle increases, the separation point gradually shifts forward. Herein, the flat hydrofoil has a yaw angle of 20° , so there is a higher likelihood of a separation region forming at the LE because of the

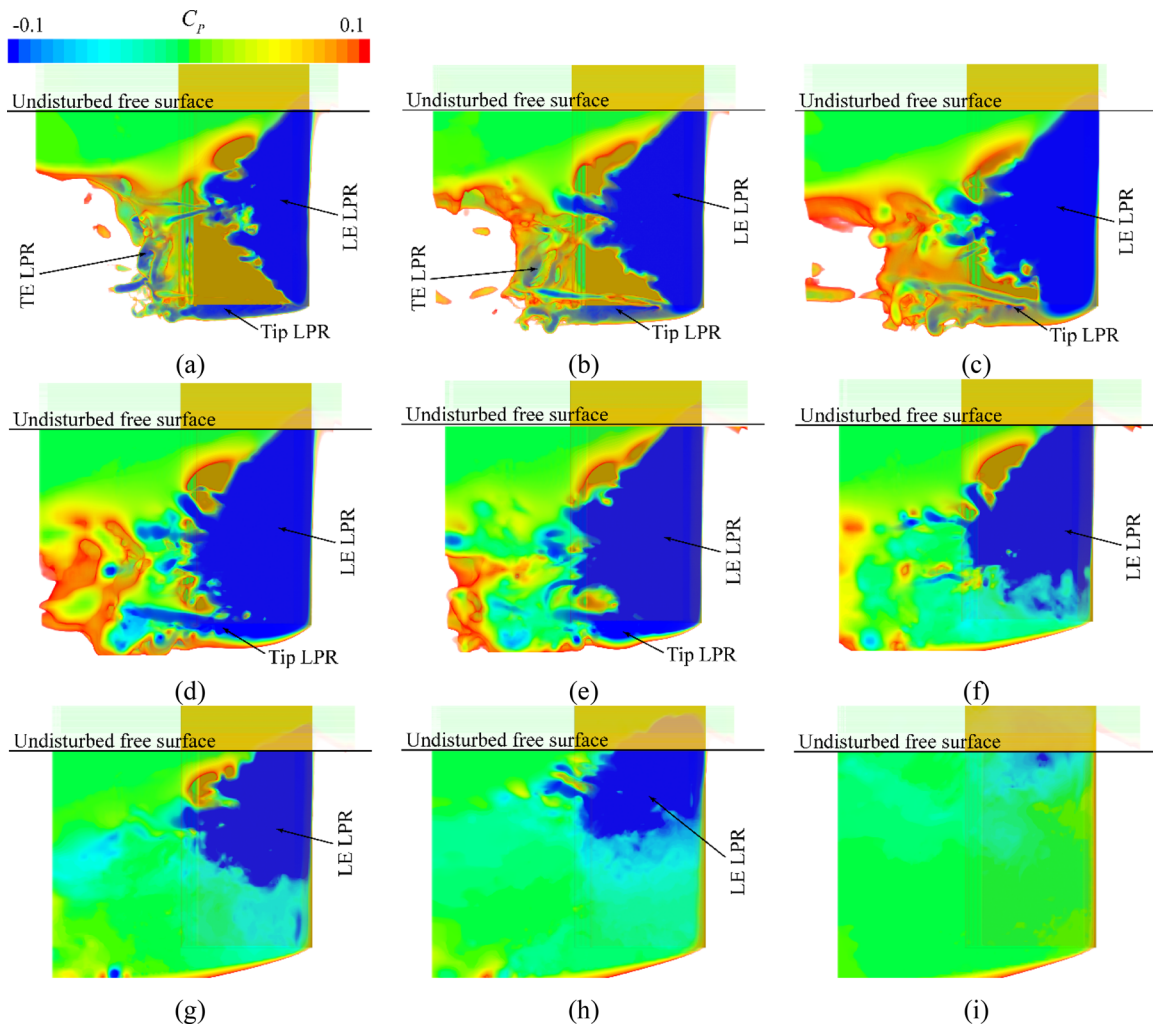


FIG. 9. Pressure distributions at various instants. LPR denotes low-pressure region: (a) t_0 , (b) $t_1 = t_0 + 0.05$ s, (c) $t_2 = t_0 + 0.1$ s, (d) $t_3 = t_0 + 0.15$ s, (e) $t_4 = t_0 + 0.175$ s, (f) $t_5 = t_0 + 0.2$ s, (g) $t_6 = t_0 + 0.225$ s, (h) $t_7 = t_0 + 0.25$ s, and (i) $t_8 = t_0 + 0.3$ s.

adverse pressure gradients. This low-pressure separation region has a notable impact on the ventilation behavior and should be considered in future hydrofoil designs to optimize hydrodynamic performance and mitigate potential adverse effects on ventilation.

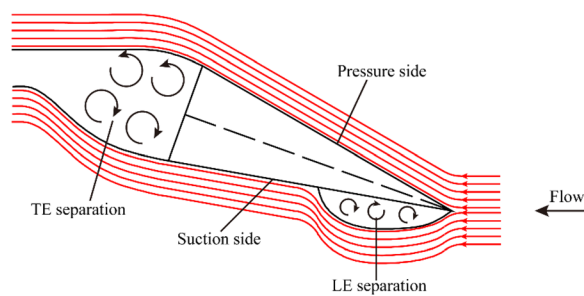


FIG. 10. Separation regions at the leading edge (LE) and trailing edge (TE) of the hydrofoil.

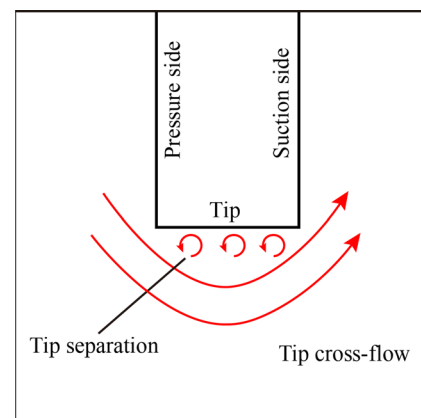


FIG. 11. Hydrofoil tip separation region.

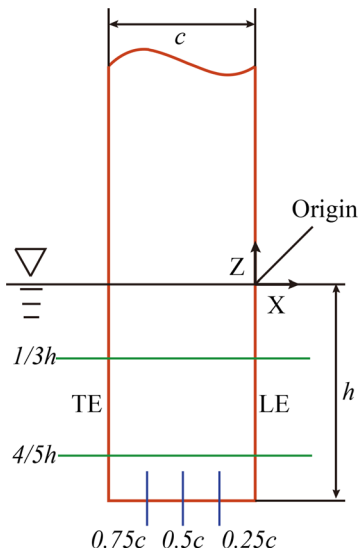


FIG. 12. Cross-sectional positions.

Figures 15 and 16 illustrate the streamlines, pressure, and velocity distributions at various sections of the hydrofoil tip at time t_5 , which is at the beginning of the SSV formation stage. From these distributions, the following insight can be gained.

The fluid near the hydrofoil tip exhibits a flow pattern from the PS to the SS, known as tip cross-flow (Fig. 11). This phenomenon occurs because of the substantial pressure difference between the two sides of the hydrofoil.

The presence of a local LPR near the hydrofoil tip leads to the generation of backflow together with a vortex, creating complex flow patterns. As the fluid transitions from PS to SS, it undergoes a gradual reduction in velocity under the frictional resistance and shear forces along the hydrofoil tip wall, as depicted in Fig. 16. This process contributes to the formation of a stable vortex structure, where shear energy is continuously transferred to the backflow. The vortex structure, in turn, generates a localized low-pressure region around the hydrofoil tip (Fig. 15). This intricate flow behavior has significant implications for the ventilation process and the hydrofoil's overall performance.

D. Effect of ventilation on vortex evolution

The vortex structure surrounding the hydrofoil allows us to comprehend the hydrofoil's ventilation formation process. The Q criterion⁵² facilitates the visualization of the spatial structure of vortices around the hydrofoil, enabling a comprehensive study of flow separation and the influence of turbulence on the vortical structure evolution. It is mathematically defined as follows:

$$Q = \frac{1}{2}(\Omega^2 - S^2), \tag{16}$$

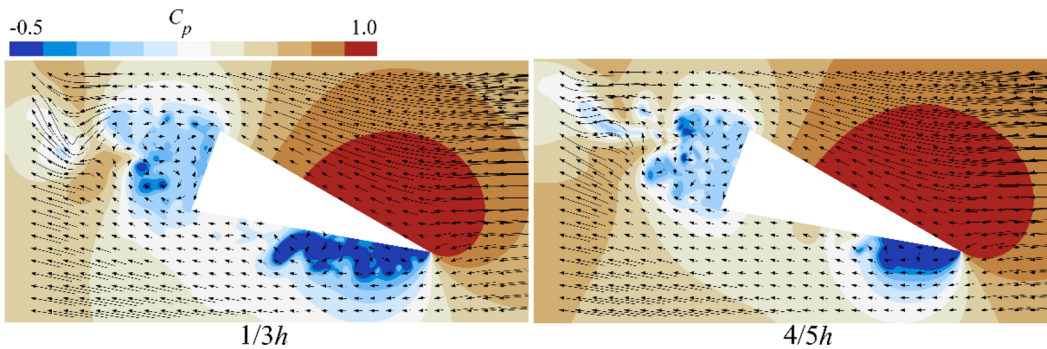


FIG. 13. Pressure distributions at t_0 .

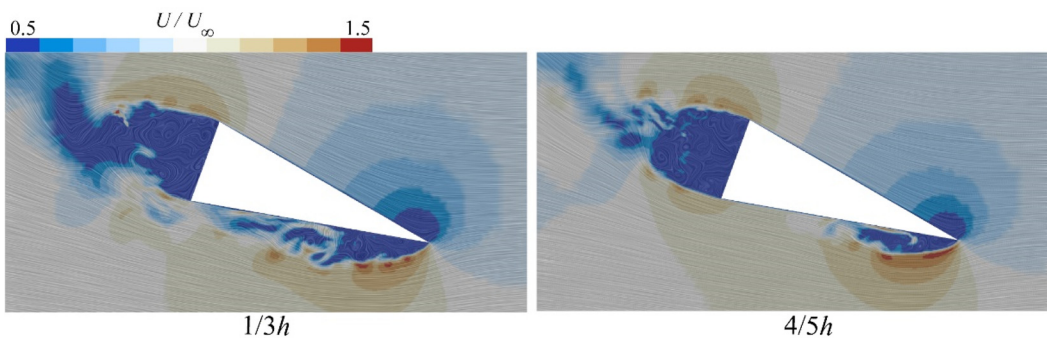


FIG. 14. Velocity distributions at t_0 .

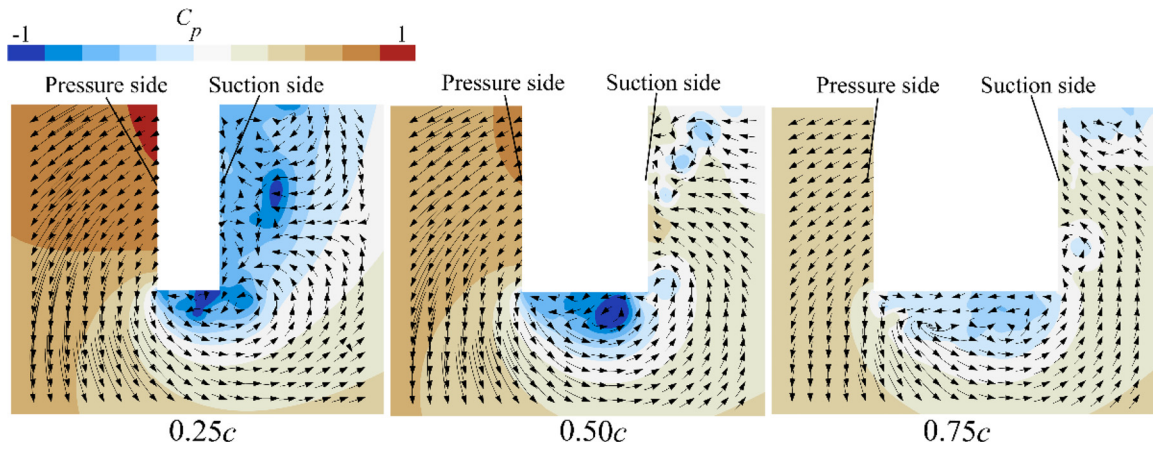


FIG. 15. Pressure distributions at three sections ($t_5 = t_0 + 0.2$ s).

where Q represents the second invariant of the velocity gradient tensor, Ω denotes the vorticity tensor, and S is the rate-of-strain tensor.⁵³ When $Q > 0$, the vorticity is dominant in the specific region, classifying it as a vortex core region. When $Q < 0$, the strain rate tensor is dominant in this region, categorizing it as a high-strain region.

In Fig. 17, the vortical structures are depicted using the isosurface of $Q = 100 \text{ s}^{-2}$, which consists primarily of the tip vortex, hydrofoil TE separation vortex, and hydrofoil LE separation vortex. The ventilation process significantly affects the vortex structure near the hydrofoil.

- (1) In Fig. 17(a), flow separation at the hydrofoil's blunt TE generates a TE separation vortex with three-dimensional vortical structures. Subsequently, as the air continues to enter accompanied by BV cavity generation and expansion, the TE separation vortex gradually develops and spreads downstream.
- (2) In Figs. 17(a)–17(c), a tip-leakage vortex (TLV) and a tip-separation vortex (TSV) appear at the hydrofoil tip; these structures exist independently. However, as air reaches the hydrofoil tip [Fig. 17(c)], the TLV and TSV draw in air from the

ventilated cavity and rapidly expand, before merging to form a strong and stable tip vortex [Fig. 17(d)].

- (3) The LE separation vortex is primarily associated with the separated flow at the LE and exhibits a parabolic shape. In Figs. 17(a)–17(e), the LE separation vortex extends toward the TE and is unchanged during the BV and TVV stages. However, with the rapid expansion of the aerated cavity from the hydrofoil tip toward the free surface along the suction surface [Figs. 17(f)–17(i)], the LE separation vortex gradually develops downstream and dissipates under the influence of the SSV flow.

To analyze the interactions between the ventilated cavity and vortex, the vorticity transport equation^{54,55} is used to quantify the vorticity transport during the ventilation formation process:

$$\frac{D\omega}{Dt} = (\omega \cdot \nabla)\mathbf{u} - \omega(\nabla \cdot \mathbf{u}) + \frac{1}{\rho_m^2}(\nabla \rho_m \times \nabla p) + (\nu_m + \nu_t)\nabla^2\omega, \tag{17}$$

where ω represents the vorticity. The first term is the stretching term, which accounts for the change in the magnitude and direction of the

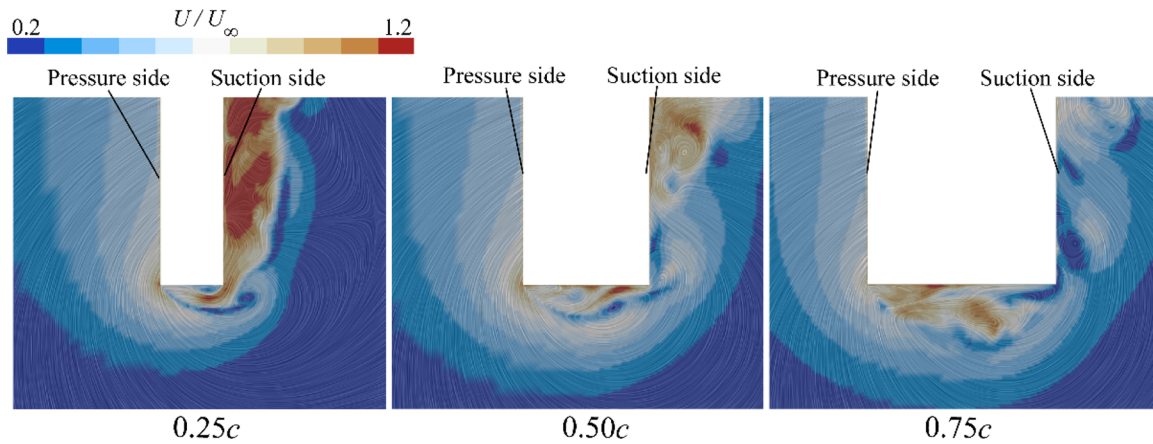


FIG. 16. Velocity distributions at three sections ($t_5 = t_0 + 0.2$ s).

21 October 2024 06:19:15

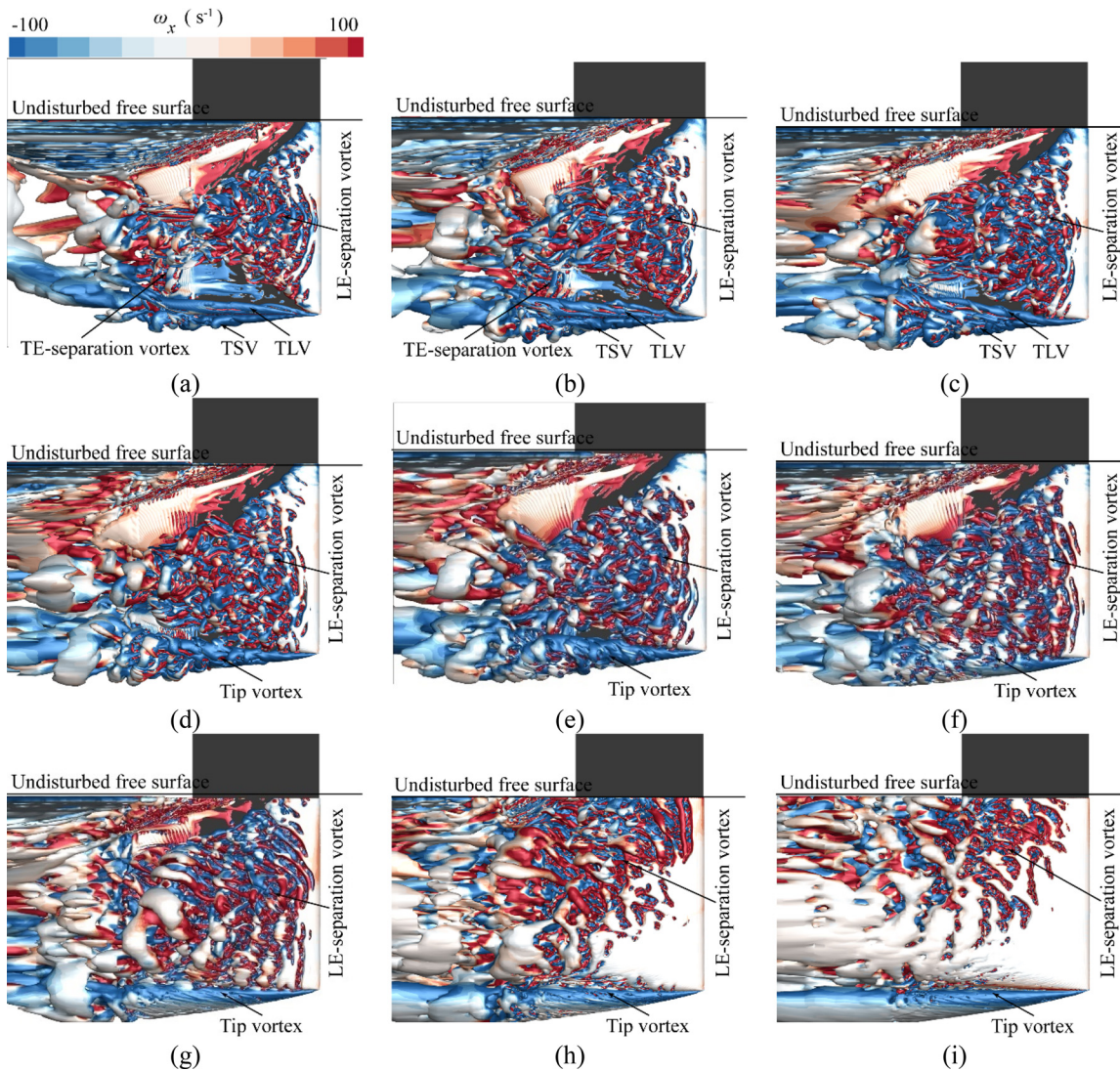


FIG. 17. Vortical structures around the surface-piercing hydrofoil. Isosurface is extracted via contour $Q = 100 \text{ s}^{-2}$ and colored via pressure coefficients: (a) t_0 , (b) $t_1 = t_0 + 0.05 \text{ s}$, (c) $t_2 = t_0 + 0.1 \text{ s}$, (d) $t_3 = t_0 + 0.15 \text{ s}$, (e) $t_4 = t_0 + 0.175 \text{ s}$, (f) $t_5 = t_0 + 0.2 \text{ s}$, (g) $t_6 = t_0 + 0.225 \text{ s}$, (h) $t_7 = t_0 + 0.25 \text{ s}$, (i) $t_8 = t_0 + 0.3 \text{ s}$.

vorticity induced by velocity variations in the flow field.⁵⁶ The second term is the dilatation term, which captures the influence of fluid compressibility on the vorticity due to fluid expansion and contraction. The third term is the baroclinic torque term, which considers the influence of the pressure and density gradients on vorticity.⁵⁷ The fourth term is the vortex-viscosity term, which considers the influence of viscous dissipation on vorticity. As the magnitude of the fourth term is relatively small when compared with that of the other three terms, it is neglected in the following analysis.

Figures 18–20 show the distributions of the stretching term, dilatation term, and baroclinic torque term in the longitudinal section and the hydrofoil SS at different instants. The subsequent discussion focuses on the Y component in the vorticity-transport equation, i.e.,

$$[(\boldsymbol{\omega} \cdot \nabla)\mathbf{u}]_Y = \omega_X \frac{\partial u_Y}{\partial X} + \omega_Y \frac{\partial u_Y}{\partial Y} + \omega_Z \frac{\partial u_Y}{\partial Z}, \quad (18)$$

$$[\boldsymbol{\omega}(\nabla \cdot \mathbf{u})]_Y = \omega_Y \left(\frac{\partial u_X}{\partial X} + \frac{\partial u_Y}{\partial Y} + \frac{\partial u_Z}{\partial Z} \right), \quad (19)$$

$$\left[\frac{1}{\rho_m^2} (\nabla \rho_m \times \nabla p) \right]_Y = \frac{1}{\rho_m^2} \left(\frac{\partial \rho_m}{\partial Z} \cdot \frac{\partial p}{\partial X} - \frac{\partial \rho_m}{\partial X} \cdot \frac{\partial p}{\partial Z} \right), \quad (20)$$

where ω_X , ω_Y , and ω_Z are the vorticity components in each coordinate axis direction.⁵⁴

$$\omega_X = \frac{\partial u_Z}{\partial Y} - \frac{\partial u_Y}{\partial Z}, \quad \omega_Y = \frac{\partial u_X}{\partial Z} - \frac{\partial u_Z}{\partial X}, \quad \omega_Z = \frac{\partial u_Y}{\partial X} - \frac{\partial u_X}{\partial Y}. \quad (21)$$

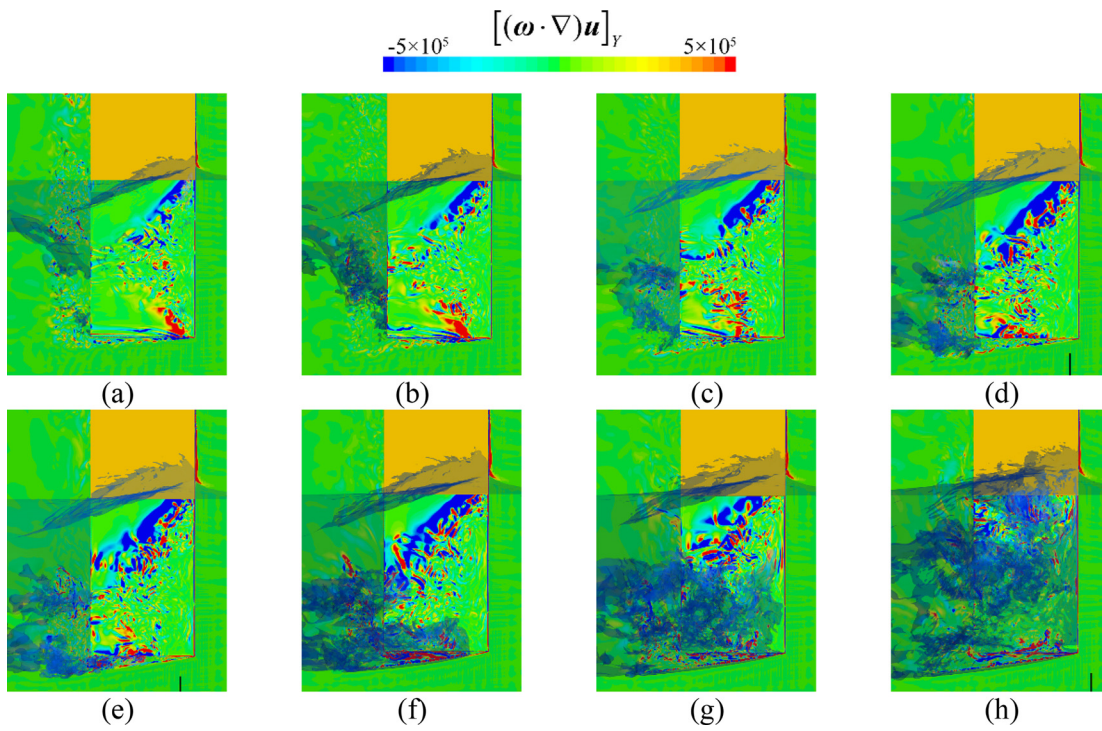


FIG. 18. Evolution of vorticity stretching term in the Y-direction at various instants: (a) t_0 , (b) $t_1 = t_0 + 0.05$ s, (c) $t_2 = t_0 + 0.1$ s, (d) $t_3 = t_0 + 0.15$ s, (e) $t_4 = t_0 + 0.175$ s, (f) $t_5 = t_0 + 0.2$ s, (g) $t_6 = t_0 + 0.225$ s, and (h) $t_7 = t_0 + 0.25$ s.

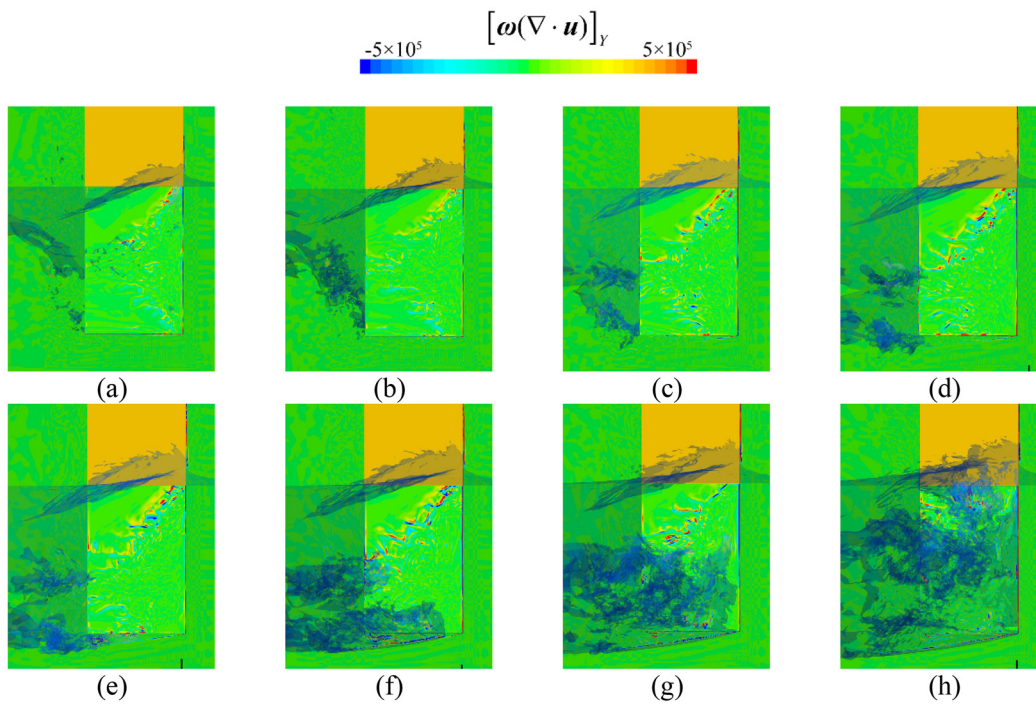


FIG. 19. Evolution of vorticity dilatation term in the Y-direction at various instants: (a) t_0 , (b) $t_1 = t_0 + 0.05$ s, (c) $t_2 = t_0 + 0.1$ s, (d) $t_3 = t_0 + 0.15$ s, (e) $t_4 = t_0 + 0.175$ s, (f) $t_5 = t_0 + 0.2$ s, (g) $t_6 = t_0 + 0.225$ s, and (h) $t_7 = t_0 + 0.25$ s.

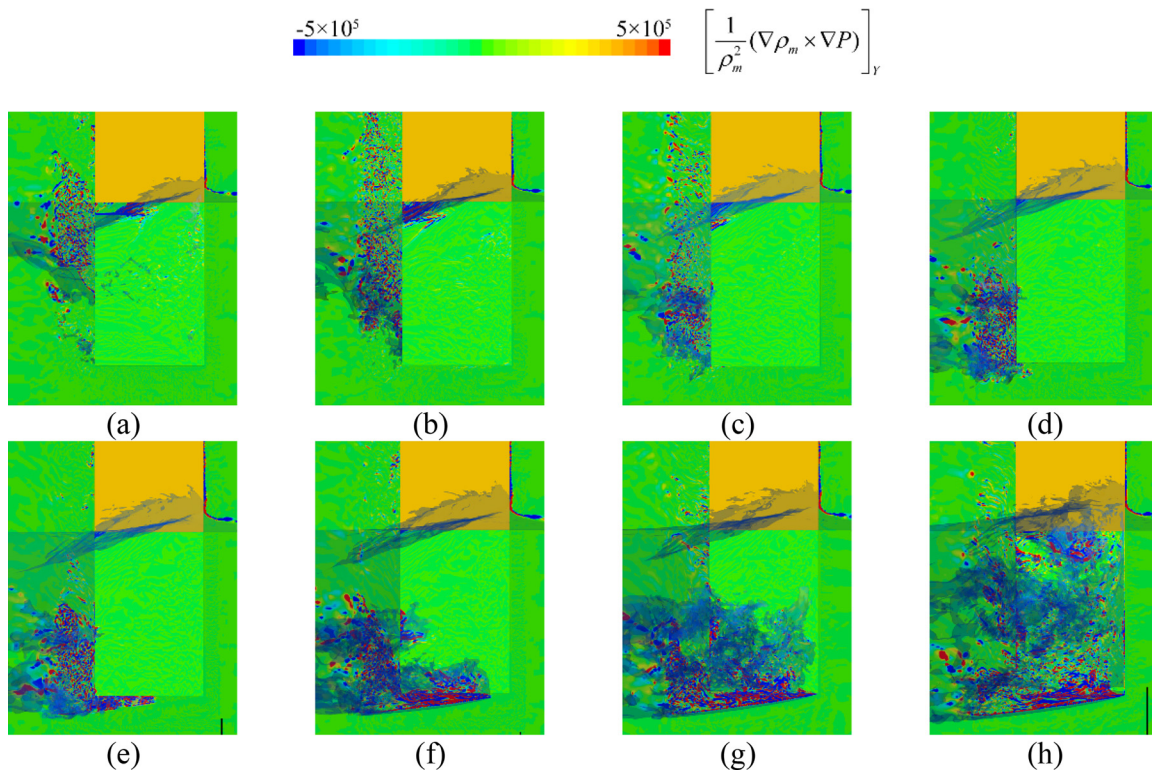


FIG. 20. Evolution of vorticity baroclinic torque term in the Y-direction at various instants: (a) t_0 , (b) $t_1 = t_0 + 0.05$ s, (c) $t_2 = t_0 + 0.1$ s, (d) $t_3 = t_0 + 0.15$ s, (e) $t_4 = t_0 + 0.175$ s, (f) $t_5 = t_0 + 0.2$ s, (g) $t_6 = t_0 + 0.225$ s, and (h) $t_7 = t_0 + 0.25$ s.

Figure 18 illustrates the evolution of the vorticity stretching term at various instants. In the BV stage [Figs. 18(a)–18(c)], the vorticity stretching term is evident at the hydrofoil’s suction surface and has a parabolic shape, which corresponds to the interface of the stall-induced flow separation region. The vorticity stretching term can also be observed around the hydrofoil tip. With the acceleration of the hydrofoil, the stretching term starts to affect a larger area, including the hydrofoil’s SS and tip. In the TVV stage [Figs. 18(d) and 18(e)] and the SSV stage [Figs. 18(f)–18(h)], the vortex stretching term has a stronger effect on the hydrofoil SS and tip.

Throughout the process of ventilation formation, the stretching term is significantly influenced by the cavity itself, leading to a gradual increase in the size of the affected region. This phenomenon arises because the stretching term depends on the velocity gradient, and the ventilated cavity changes the velocity field around the hydrofoil, thereby affecting the velocity gradient distribution.

During the initial stages, when the cavity is relatively small, changes in the vortex stretching term at the hydrofoil’s SS and tip primarily result from alterations in the velocity gradient caused by the hydrofoil’s acceleration. As the hydrofoil speed further increases, the aerated cavity expands, and the velocity gradient within the cavity becomes relatively small compared with the velocity gradient induced by the surrounding water.

Figure 19 illustrates the evolution of the vorticity dilatation term during acceleration. It is evident that the dilatation term has a minimal impact on the vortical structures, and its range of influence is smaller

than the other two terms. The primary influence of the dilatation term is on the hydrofoil’s suction surface, because vortex dilatation is directly associated with velocity divergence.

Figure 20 depicts the evolution of the vorticity baroclinic torque term during acceleration. The ventilated cavity clearly has a significant effect on the baroclinic torque term, which primarily exists at the interface between air and water and undergoes changes during the ventilation formation process. The region of influence of the vortex baroclinic torque aligns with the path of ventilated cavity development, starting from the hydrofoil’s TE, then extending to the hydrofoil tip, and finally reaching the hydrofoil’s SS.

Due to the substantial difference in density between water and air (~ 800 times), the density gradient at the interface between the ventilated cavity and the water fluid is no longer parallel to the pressure gradient.^{58,59} Compared with the vortex stretching and dilatation terms, the vortex baroclinic torque term has a greater effect, and ventilation leads to a more complex and stronger form of the vortex baroclinic torque.

The results indicate that, during hydrofoil ventilation, the vorticity is primarily influenced by vortex stretching and baroclinic torque. The dilatation term has a minimal effect, whereas the baroclinic torque term exerts the greatest influence.

IV. CONCLUSIONS

In this study, the ventilation formation induced by tip vortices ($AR_h = 1.5$, $\beta = 20^\circ$, $Fr_h = 0.93\text{--}3.15$) was numerically investigated

over a surface-piercing hydrofoil. Several fundamental insights into the transient flow characteristics, hydrodynamic loads, and effects of ventilation on the flow structures and vortex evolution were discussed and analyzed.

- (1) These numerical results demonstrate good agreement with our experimental observations. The present simulation approach can capture typical flow features, including the existence of tip vortices, the ventilated cavity with PS spray, and their evolution.
- (2) The process of tip-vortex-induced ventilation formation involves three sequential stages, namely, base ventilation (BV), tip-vortex ventilation (TVV), and suction-side ventilation (SSV). Specifically, air begins to penetrate downward along the blunt TE and then flows upstream through the tip vortex. The aerated cavity quickly expands upward along the hydrofoil's suction surface, ultimately forming a fully ventilated flow that completely envelops the hydrofoil. Moreover, the inertia force causes the PS spray to rise continuously, forming a wave crest before freely falling to the water surface in the far field.
- (3) Compared with the drag coefficient, ventilation has a greater impact on the lift coefficient. The lift coefficient increases during the BV and TVV stages because of the expansion of the low-pressure separation region on the suction surface, causing a gain in pressure difference on both sides of the hydrofoil. Subsequently, in the SSV stage, the LPR is gradually replaced by a ventilated cavity with atmospheric pressure, causing a reduction in the pressure difference on both sides as well as the lift coefficient.
- (4) The vortical structures around the hydrofoil consist of the tip vortex, TE separation vortex, and LE separation vortex. The tip-leakage vortex (TLV) and tip-separation vortex (TSV) initially exist independently at the hydrofoil tip, then expand and merge through air ventilation, ultimately forming a strongly stable tip vortex.
- (5) During the process of ventilation formation, the vorticity generation and transportation are primarily induced by vortex stretching and baroclinic torque. The baroclinic torque term has the greatest effect and is closely related to the evolution of the aerated cavity; the vortex stretching term has the next-strongest effect, and the dilatation effect has the least effect.

ACKNOWLEDGMENTS

The authors would like to gratefully acknowledge the National Natural Science Foundation of China (Nos. 52006232 and U22B6010), the international partnership program of Chinese Academy of Sciences (Grant No. 025GJHZ2022118FN).

AUTHOR DECLARATIONS

Conflict of Interest

The authors have no conflicts to disclose.

Author Contributions

Yuchang Zhi: Conceptualization (equal); Formal analysis (lead); Investigation (lead); Methodology (lead); Writing – original draft (lead). **Renfang Huang:** Conceptualization (lead); Funding acquisition

(lead); Resources (equal); Supervision (lead); Writing – review & editing (lead). **Rundi Qiu:** Formal analysis (supporting); Investigation (equal); Methodology (supporting). **Yiwei Wang:** Conceptualization (supporting); Resources (lead); Supervision (equal). **Qun Sun:** Resources (supporting); Supervision (supporting). **Shuting Cai:** Software (supporting); Visualization (supporting).

DATA AVAILABILITY

The data that support the findings of this study are available from the corresponding author upon reasonable request.

REFERENCES

- ¹R. J. Yan, S. Pang, H. B. Sun, and Y. J. Pang, "Development and missions of unmanned surface vehicle," *J. Mar. Sci. Appl.* **9**(4), 451–457 (2010).
- ²Z. Liu, Y. Zhang, X. Yu, and C. Yuan, "Unmanned surface vehicles: An overview of developments and challenges," *Annu. Rev. Control* **41**, 71–93 (2016).
- ³X. Bi, *Overview of Autonomous Unmanned Systems* (Springer, Singapore, 2021).
- ⁴M. F. Platzer and N. Sarigul-Klijn, *Major Elements and Developmental Status of the Energy Ship Concept* (Springer International Publishing, Cham, 2021).
- ⁵M. A. Budiyo, N. Y. Prawira, and H. Dwiputra, "Lift-to-drag ratio of the application of hydrofoil with variation mounted position on high-speed patrol vessel," *CFD Lett.* **13**(5), 1–9 (2021).
- ⁶M. Basic, B. Šarić, J. Basic, and B. Blagojević, "CFD analysis of surface-piercing hydrofoil ventilation inception," in *XXII. Symposium Sorta* (2016).
- ⁷S. Brizzolara and Y. L. Young, "Physical and theoretical modeling of surface-piercing hydrofoils for a high-speed unmanned surface vessel," in *International Conference on Offshore Mechanics and Arctic Engineering* (2012).
- ⁸A. Damley-Strnad, C. Harwood, and Y. L. Young, "Hydrodynamic performance and hysteresis response of hydrofoils in ventilated flows," in *Sixth International Symposium on Marine Propulsors* (2019).
- ⁹J. P. Breslin and R. Skalak, "Exploratory study of ventilated flows about yawed surface-piercing struts," Report No. 2-23-59W (NASA, Washington, DC, 1959).
- ¹⁰Y. C. Zhi, J. M. Zhan, R. F. Huang, R. D. Qiu, and Y. W. Wang, "Numerical investigations into the ventilation elimination mechanism of a surface-piercing hydrofoil," *Ocean Eng.* **243**, 110225 (2022).
- ¹¹E. Pogozelski, J. Katz, and T. Huang, "The flow structure around a surface piercing strut," *Phys. Fluids* **9**(5), 1387–1399 (1997).
- ¹²R. S. Rothblum, *Investigation of Methods of Delaying or Controlling Ventilation on Surface Piercing Struts* (University of Leeds, 1977).
- ¹³R. L. Waid, "Experimental investigation of the ventilation of vertical surface-piercing struts in the presence of cavitation," Report No. AD0738493 (Naval Ship Research and Development Center, Sunnyvale, CA, 1968).
- ¹⁴R. S. Rothblum, D. A. Mayer, and G. M. Wilburn, "Ventilation, cavitation and other characteristics of high speed surface-piercing struts," Report No. 3023 (Naval Ship Research and Development Center, Washington, DC, 1969).
- ¹⁵P. Swales, A. Wright, R. McGregor, and R. Rothblum, "The mechanism of ventilation inception on surface piercing foils," *J. Mech. Eng. Sci.* **16**(1), 18–24 (1974).
- ¹⁶C. M. Harwood, K. A. Brucker, F. Miguel, Y. L. Young, and S. L. Ceccio, "Experimental and numerical investigation of ventilation inception and wash-out mechanisms of a surface-piercing hydrofoil," in 30th Symposium on Naval Hydrodynamics, Hobart, Tasmania, Australia, 2014.
- ¹⁷C. M. Harwood, Y. L. Young, and S. L. Ceccio, "Ventilated cavities on a surface-piercing hydrofoil at moderate Froude numbers: Cavity formation, elimination and stability," *J. Fluid Mech.* **800**, 5–56 (2016).
- ¹⁸Y. L. Young, C. M. Harwood, F. Miguel, J. C. Ward, and S. L. Ceccio, "Ventilation of lifting bodies: Review of the physics and discussion of scaling effects," *Appl. Mech. Rev.* **69**(1), 010801 (2017).
- ¹⁹C. M. Harwood, M. Felli, M. Falchi, S. L. Ceccio, and Y. L. Young, "The hydroelastic response of a surface-piercing hydrofoil in multi-phase flows. Part 1. Passive hydroelasticity," *J. Fluid Mech.* **881**, 313–364 (2019).
- ²⁰C. M. Harwood, M. Felli, M. Falchi, N. Garg, S. L. Ceccio, and Y. L. Young, "The hydroelastic response of a surface-piercing hydrofoil in multiphase flows.

- Part 2. Modal parameters and generalized fluid forces,” *J. Fluid Mech.* **884**, A3 (2019).
- ²¹R. Huang, R. Qiu, Y. Zhi, and Y. Wang, “Investigations into the ventilated cavities around a surface-piercing hydrofoil at high Froude numbers,” *Phys. Fluids* **34**(4), 043304 (2022).
- ²²Y. Wang, R. Huang, R. Qiu, Y. Wang, and T. Du, “Experimental study on the mechanism of cavitation-induced ventilation,” *Int. J. Multiphase Flow* **170**, 104633 (2024).
- ²³L. Wang, P. Wang, K. Wu, H. Wang, B. Huang, and D. Wu, “Experiment investigation of the tip vortex cavitation around a pitching hydrofoil,” *Phys. Fluids* **35**(10), 103313 (2023).
- ²⁴Z. Li, Z. Zuo, and Z. Qian, “Diffusion-driven periodic cavitation bubbling from a Harvey-type crevice in shear flows,” *Phys. Fluids* **35**(10), 102112 (2023).
- ²⁵Y. D. Hu, C. Liu, C. H. Hu, and D. C. Wan, “Numerical investigation of flow structure and air entrainment of breaking bow wave generated by a rectangular plate,” *Phys. Fluids* **33**(12), 122113 (2021).
- ²⁶D. Zhang, J. Zhang, T. Sun, and Y. Jiang, “Ventilated cavity dynamics of an axisymmetric body under the influence of a structure,” *Phys. Fluids* **35**, 055112 (2023).
- ²⁷B. Tian, B. Huang, and L. Li, “Investigation of transient sheet/cloud cavitating flow dynamics from multiscale perspective,” *Phys. Fluids* **35**(7), 077115 (2023).
- ²⁸M. Charlou, J. Wackers, G. B. Deng, E. Guilmineau, A. Leroyer, P. Queutey, and M. Visonneau, “Assessing bi-stable ventilation for surface-piercing hydrofoils through numerical simulation,” in *Innov’Sail 2020* (2020).
- ²⁹K. I. Matveev, M. P. Wheeler, and T. Xing, “Simulations of an air-ventilated strut crossing water surface at variable yaw angles,” in *Fluids Engineering Division Summer Meeting* (American Society of Mechanical Engineers, 2018).
- ³⁰M. Andrun, B. Blagojević, J. Bašić, and B. Klarin, “Impact of CFD simulation parameters in prediction of ventilated flow on a surface-piercing hydrofoil,” *Ship Technol. Res.* **68**(1), 1–13 (2021).
- ³¹S. Brizzolara and D. Villa, “Three phases RANSE calculations for surface-piercing super-cavitating hydrofoils,” in *8th International Symposium on Cavitation CAV2012*, Singapore, 2012.
- ³²Y. Shi, S. Gao, G. Pan, and X. Quan, “RANS/LES investigation on the performance of air film fusion around a vertically launched underwater vehicle,” *Ocean Eng.* **266**, 112880 (2022).
- ³³Y. Zhi, R. Huang, R. Qiu, Y. Wang, and C. Huang, “LES investigation into the cavity shedding dynamics and cavitation–vortex interaction around a surface-piercing hydrofoil,” *Phys. Fluids* **34**(12), 123314 (2022).
- ³⁴Y. Wang, C. Huang, T. Du, R. Huang, Y. Zhi, Y. Wang, Z. Xiao, and Z. Bian, “Research on ventilation and supercavitation mechanism of high-speed surface-piercing hydrofoil,” *Phys. Fluids* **34**(2), 023316 (2022).
- ³⁵Z. Li, C. Liu, D. C. Wan, and C. H. Hu, “High-fidelity simulation of a hydraulic jump around a surface-piercing hydrofoil,” *Phys. Fluids* **33**(12), 123304 (2021).
- ³⁶V.-T. Nguyen, T.-H. Phan, and W.-G. Park, “Modeling of shock wave produced by collapse of cavitation bubble using a fully conservative multiphase model,” *Phys. Fluids* **35**(11), 116102 (2023).
- ³⁷X. Zhang, C. Yang, C. Wang, Y. Zhang, and Y. Zhang, “Dynamics of an oscillating cavitation bubble within a narrow gap,” *Phys. Fluids* **35**(10), 103302 (2023).
- ³⁸C. Xu and B. C. Khoo, “Dynamics of the supercavitating hydrofoil with cavitator in steady flow field,” *Phys. Fluids* **32**(12), 123307 (2020).
- ³⁹Z. Li, Z. Qian, and B. Ji, “Transient cavitating flow structure and acoustic analysis of a hydrofoil with whalelike wavy leading edge,” *Appl. Math. Model.* **85**, 60–88 (2020).
- ⁴⁰C. Xie, J. Liu, J.-W. Jiang, and W.-X. Huang, “Numerical study on wetted and cavitating tip-vortical flows around an elliptical hydrofoil: Interplay of cavitation, vortices, and turbulence,” *Phys. Fluids* **33**(9), 093316 (2021).
- ⁴¹W. Liu, Y. Kang, M. Zhang, X. Wang, and D. Li, “Self-sustained oscillation and cavitation characteristics of a jet in a Helmholtz resonator,” *Int. J. Heat Fluid Flow* **68**, 158–172 (2017).
- ⁴²W. Li, Z. Dong, W. Zhao, and X. Liang, “Numerical simulation of oil spill in the arctic ice-covered waters: focusing on different ice concentrations and wave’s impacts,” *J. Mar. Sci. Eng.* **11**(1), 114 (2023).
- ⁴³P. R. Spalart and C. L. Rumsey, “Effective inflow conditions for turbulence models in aerodynamic calculations,” *AIAA J.* **45**(10), 2544–2553 (2007).
- ⁴⁴J. T. Woeste, C. M. O’Reilly, R. K. Gouveia, and Y. L. Young, “Propeller–hull interactions and added power in head seas,” *Ocean Eng.* **247**, 110630 (2022).
- ⁴⁵S. Xia, X. Zhou, G. Hu, and X. Cao, “CFD analysis of the flow blockage in a rectangular fuel assembly of the IAEA 10 MW MTR research reactor,” *Nucl. Eng. Technol.* **53**(9), 2847–2858 (2021).
- ⁴⁶J. Choi and S. B. Yoon, “Numerical simulations using momentum source wave-maker applied to RANS equation model,” *Coastal Eng.* **56**(10), 1043–1060 (2009).
- ⁴⁷Y. Long, X. P. Long, B. Ji, W. X. Huai, and Z. D. Qian, “Verification and validation of URANS simulations of the turbulent cavitating flow around the hydrofoil,” *J. Hydrodyn.* **29**(4), 610–620 (2017).
- ⁴⁸T. S. Phillips and C. J. Roy, “Richardson extrapolation-based discretization uncertainty estimation for computational fluid dynamics,” *J. Fluids Eng.* **136**(12), 121401 (2014).
- ⁴⁹A. Satyadharma and Harinaldi, “The performance of a gradient-based method to estimate the discretization error in computational fluid dynamics,” *Computation* **9**(2), 10 (2021).
- ⁵⁰T. Smith and Y. Ventikos, “Wing-tip vortex dynamics at moderate Reynolds numbers,” *Phys. Fluids* **33**(3), 035111 (2021).
- ⁵¹L. Xin, L. Yibin, W. Bo, Z. Shengfu, J. Weimin, and L. Wanqi, “Effect of blade top clearance on semi-open fuel pump performance and leakage vortex,” *J. Braz. Soc. Mech. Sci. Eng.* **45**(6), 330 (2023).
- ⁵²J. C. R. Hunt, A. A. Wray, and P. Moin, “Eddies, streams, and convergence zones in turbulent flows,” in *Proceedings of the 1988 Summer Program*, 1988.
- ⁵³T. Sun, Z. Wang, L. Zou, and H. Wang, “Numerical investigation of positive effects of ventilated cavitation around a NACA66 hydrofoil,” *Ocean Eng.* **197**, 106831 (2020).
- ⁵⁴A. Yu, Z. Qian, X. Wang, Q. Tang, and D. Zhou, “Large Eddy simulation of ventilated cavitation with an insight on the correlation mechanism between ventilation and vortex evolutions,” *Appl. Math. Model.* **89**, 1055–1073 (2021).
- ⁵⁵H. Cheng, X. Bai, X. Long, B. Ji, X. Peng, and M. Farhat, “Large eddy simulation of the tip-leakage cavitating flow with an insight on how cavitation influences vorticity and turbulence,” *Appl. Math. Model.* **77**, 788–809 (2020).
- ⁵⁶J. Li, C. Liu, Z. Ran, and B. Chai, “Numerical investigation of unsteady cavitating turbulent flows around a three-dimensional hydrofoil using stress-blended eddy simulation,” *Proc. Inst. Mech. Eng., Part E* **235**(6), 1971–1983 (2021).
- ⁵⁷L. Wang, J. Lu, W. Liao, Y. Zhao, and W. Wang, “Numerical simulation of the tip leakage vortex characteristics in a semi-open centrifugal pump,” *Appl. Sci.* **9**(23), 5244 (2019).
- ⁵⁸J. Zhu, D. Zhao, L. Xu, and X. Zhang, “Interactions of vortices, thermal effects and cavitation in liquid hydrogen cavitating flows,” *Int. J. Hydrogen Energy* **41**(1), 614–631 (2016).
- ⁵⁹S. Zhang, H. Chen, and Z. Ma, “A modified filter-based model for simulation of unsteady cavitating flows around a NACA66 hydrofoil,” *Mod. Phys. Lett. B* **35**(1), 2150032 (2021).